Dynamic imprinting of nanoscale topological phases into an antiferromagnet

Miina Leiviskä, Sarah Jenkins, Richard F. L. Evans, Daria Gusakova, Vincent Baltz

Dynamic imprinting of nanoscale topological phases into an antiferromagnet

Miina Leiviskä,[1] Sarah Jenkins,[2] Richard F. L. Evans,[2] Daria Gusakova,[1] and Vincent Baltz[1]

[1]*Univ. Grenoble Alpes, CNRS, CEA, Grenoble INP, IRIG-Spintec, F-38000 Grenoble, France*

[2]*School of Physics, Engineering and Technology, University of York, York YO10 5DD, United Kingdom*

Controlling the magnetic order of antiferromagnets is challenging due to the vanishing net magnetisation. For this reason, the study of topologically protected real-space states of antiferromagnets is restricted by the difficulty in nucleating such states. Here, using atomistic simulations we demonstrate how to nucleate predefined, localised spin textures in a thin film antiferromagnet, γ-$IrMn_3$. Utilising the exchange bias coupling between a ferromagnet and an antiferromagnet, we imprint the topological states on the former onto the latter by means of a thermal cycling procedure. The imprinted textures are shown to be stable against field perturbations. We also discuss how various material parameters affect the efficiency of the imprinting and the characteristics of the imprinted textures. This work paves way for further studies on topologically protected real-space phases in antiferromagnets and promotes the development of denser and faster spintronic devices.

The interest in topologically protected states in condensed matter physics is founded on their robustness against small perturbations as well as their significant impact on the physical properties of the system. In magnetic materials topological states can refer either to the spin-resolved topology of the energy bands in the reciprocal space, or to the spin textures in real-space. The impact of topology on the physical properties is related to the global or local symmetry of the system allowing a non-zero geometric phase [1, 2] that the electrons will acquire when interacting with the global or local spin structure. In compensated magnetic materials the multiple-oriented magnetic sublattices allow for unique symmetries and thus unique topological effects beyond those possible for traditional single-sublattice ferromagnets. For example, it has been shown recently that spin symmetries specific to multisublattice systems can give rise to novel band topologies [3, 4] that allow unexpected transport phenomena such as spontaneous anomalous Hall effect (AHE) [5–7] and spin current generation [8–10]. Considering the favourable and technologically relevant properties [11] of compensated magnets, extending the study of topology from ferromagnets to compensated

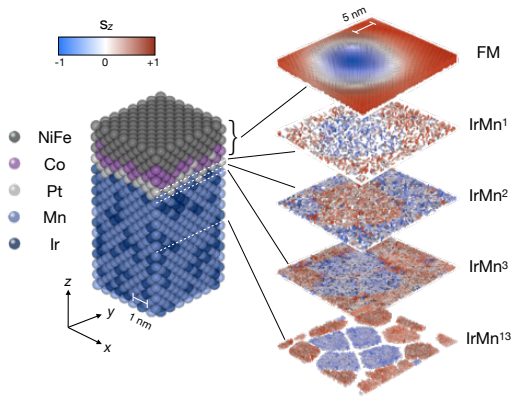

FIG. 1. (Color Online) (Left) Atomic structure of a slice of the simulation system consisting of a hybrid NiFe/Co/Pt FM single crystal coupled to a granular γ-$IrMn_3$ AFM, across an atomically intermixed interface. The full size of the simulation system is $100 \times 100 \times 6.67$ nm. (Right) Cross-section of the spin texture obtained in the FM and at several depths in the AFM, following a thermal cycling procedure. The numbers indicate the relative position of the AFM monolayers away from the interface.

magnets [12] is of significant research interest.

The real-space topological states in antiferromagnets (AFMs) such as AFM skyrmions (AF Sk) are spin textures that cannot be continuously transformed into the topologically trivial state and are therefore topologically protected. Due to the anti-parallel interatomic exchange interactions AFM Sks have both zero net magnetisation and zero topological charge, which ensure robustness against external fields and vanishing skyrmion [13, 14] and topological Hall effects [15]. Other predicted effects of AFM Sks on the transport properties include the non-vanishing topological spin Hall effect [15, 16] and a longitudinal skyrmion velocity exceeding that of the FM Sks [13, 14]. These properties make AFM Sks not only fascinating subjects for topology studies but also competitive information carrier candidates for ultra-dense, ultra-fast, low-power spintronic devices. However, due to the lack of net magnetisation, the main barrier to accessing all these advantageous properties is the difficulty in experimentally nucleating AFM Sks. So far, a few possible nucleation techniques have been proposed including conversion of a pair of AFM domain walls using vertical spin-polarized current[13] and ultrafast laser pulses [17].

Here, we use atomistic simulations to demonstrate a nucleation method that does not require complex device geometries and is applicable beyond metallic AFMs. Taking advantage of the exchange bias coupling between a FM and an AFM, we imprint the topologically protected states of

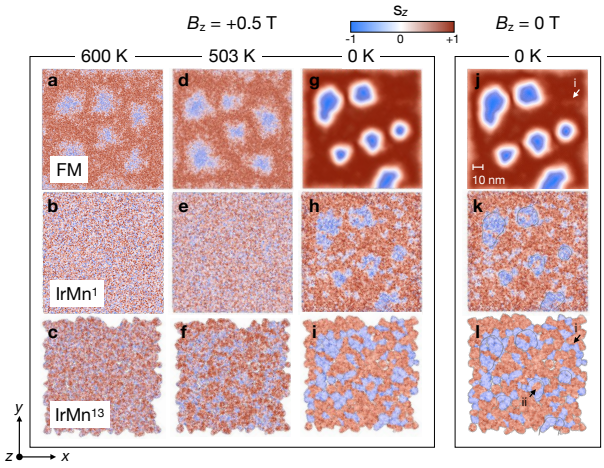

FIG. 2. (Color Online) (Left Panel) Top view snapshots of the evolution of the spin textures in the FM (Top row), AFM at the interface (Middle row, IrMn 1) and AFM in the core (Bottom row, IrMn 13), under out-of-plane field-cooling (H_z=0.5 T): at 600 K, above the Néel temperature T_N of the AFM; at 503 K, near T_N; and 0 K below T_N. (Right Panel) The spin textures at remanence, for H_z=0 T. The contours of the textures in j) are superimposed to k) and l), as visual guides.

the former onto the latter during its magnetic ordering by means of a thermal cycling procedure. This method follows previous experimental works on vortices [18, 19], and bubbles [20]. Figure 1 shows the imprinting of a Sk from a FM layer [$Ni_{80}Fe_{20}$ (0.87 nm)/Co (0.33 nm)/Pt (0.47 nm)] onto and through an AFM layer [γ-$IrMn_3$ (5 nm)], following thermal cycling. The simulation stack is based on an experimental one that has been optimised for the nucleation of Sks in the FM layer [20, 21]: the ultrathin Co/Pt bilayer provides a strong interfacial Dzyaloshinskii-Moriya interaction (DMI) [22] and some perpendicular surface magnetic anisotropy, while the thickness of the NiFe layer allows the vanishing of the total anisotropy. The magnetic coupling between the FM and AFM layers is preserved due to finite atomic intermixing. For the AFM layer we use the non-collinear γ-$IrMn_3$, due to its large exchange bias coupling originating from the statistical imbalance of spins in the four magnetic sublattices, which yields uncompensated interfacial spins [23]. Moreover, the four easy axes [24] of $IrMn_3$ may facilitate the magnetic moment winding that is necessary for a skyrmion formation. The magnetic properties of γ-$IrMn_3$ relating to its non-trivial spin structure have been thoroughly characterized using the atomistic simulation software package VAMPIRE [25, 26], which is also used for this work. The simulations utilised the ARCHER2 supercomputer with typical simulations running on 1024 CPU cores due to the large number of Monte Carlo time steps and large system size of around 6×10^6 spins.

The spin Hamiltonian governing the energetics of the system is given by

$$\mathscr{H} = -\sum_{i<j} J_{ij}\mathbf{S}_i \cdot \mathbf{S}_j - \frac{k_{\mathrm{N}}}{2}\sum_{i\neq j}^{z}(\mathbf{S}_i \cdot \mathbf{e}_{ij})^2 - \mathbf{D}_{ij} \cdot (\mathbf{S}_i \times \mathbf{S}_j) - \sum_i \mu_s \mathbf{S}_i \cdot \mathbf{B}, \tag{1}$$

The first term is the exchange interaction, where subscripts i and j refer to spins on sites i and j, J_{ij} is the exchange constant and $\mathbf{S}_i$ is the spin vector. The second term is the Néel pair anisotropy term that rotates the spins radially/tangentially to a nearest neighbor of a given element and is here used to simulate the interfacial perpendicular magnetic anisotropy (Co spins point radially to Pt sites) and correct anisotropy of $IrMn_3$ (Mn spins point tangentially to Ir sites)[24]. Here, k_{N} is the Néel pair anisotropy constant, $\mathbf{e}_{ij}$ is a unit vector and z is the number of nearest neighbors. The third term that stabilizes the topological states is the DMI interaction where $\mathbf{D}_{ij}$ is the DMI vector. The fourth term is the Zeeman energy where μ_s is the atomic magnetic moment and $\mathbf{B}$ is the external induction or flux density. The magnetic state is evolved using an adaptive Monte Carlo Metropolis algorithm [27], which is ideal for naturally simulating the temperature-dependence of the magnetic state. The simulation parameters for the different layers are listed in Supplemental Material (SM). It should be noted that the FM/Pt multilayer is a single crystal while the AFM layer is granular with an average grain size and spacing of 5 and 0.75 nm respectively, in line with experimental data [28][**?**]. The grain structure (illustrated in the SM) is created using a Voronoi construction as described previously by Jenkins *et al.* [29]. In a real polycrystalline multilayer, the FM and AFM grains are coincident and the FM grains are coupled so that it can be modelled as a single crystal. The crystal orientation of the entire simulation stack is such that the [001] crystal axis is along the film normal.

The localised AFM spin textures are nucleated by means of thermal cycling. More precisely, the simulations were carried out in three steps: i) FM Sk nucleation, ii) field-cooling, and iii) field removal. During the first step (Figure 2a-c), the system was equilibrated at 600 K in an applied field of B_z = 0.5 T parallel to the film normal, for 10^6 Monte-Carlo steps. Because 600 K is above the Néel temperature (T_N) of the AFM layer ($\sim$ 510 K, see SM) and below the Curie temperature of the FM layer ($\sim$ 900 K, see SM), this phase allows the nucleation of nanoscale Sks in the FM layer while the AFM layer remains disordered throughout. This ensures that the imprinting of spin textures is from the FM to the AFM layer and not vice versa. In the second simulation step (Figure 2d-f), the system is cooled down to 0 K in the same field in order to further stabilize the FM layer

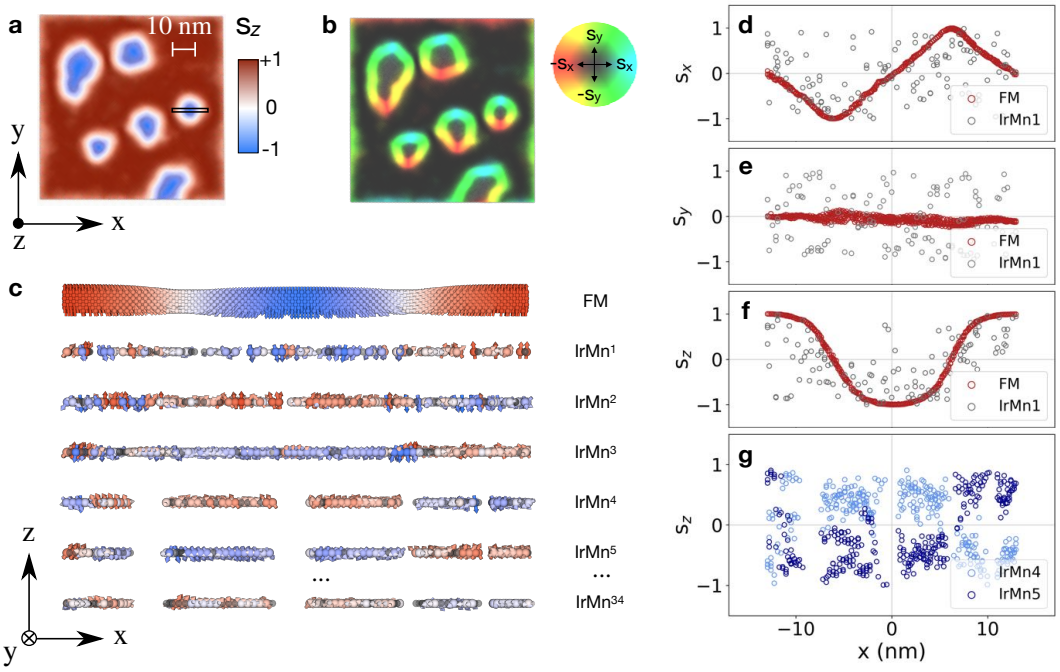

FIG. 3. (Color Online) Top view of the spin structure in the FM layer showing azimuthal (a) and rotational (b) components of the magnetization showing the existence of skyrmion-like textures in the ferromagnetic layer. (c) Layer-by-layer spin structure through the sample, corresponding to the cross-section indicated in (a) showing the propagation of the spin texture into the antiferromagnet. The spin direction alternates in the lower antiferromagnetic layers due to the antiferromagnetic coupling. (d-f) Lateral dependencies of the spin components s_i in the FM, IrMn 1, IrMn 4 and IrMn 5 layers showing the presence of domain walls in the FM and corresponding structure in the antiferromagnet.

and set the AFM layer upon crossing the Néel temperature. The bulk AFM (exemplified by IrMn 13 in Figure 2) begins to set around $T \approx 500$ K. The interfacial moments of the AFM (IrMn 1 in Figure 2), on the other hand, are subject to more thermal noise and the imprinting of the FM spin textures is difficult to discern. This is likely due to the reversible component fluctuating with the FM spins. At $T = 0$ K (Figure 2g-i), the imprinting of the FM spin textures onto the AFM interface and into the AFM bulk becomes clear: the spin textures observed in the FM are largely reproduced in the bulk AFM as highlighted by the contours in Figure 2j-l and their exact shape is governed by the grain boundaries of the AFM. Note that superimposed to the imprinted spin textures there are also random spin textures in the AFM bulk that don't correspond to the FM spin configuration. These discrepancies can be divided into two categories based on their location and the extent of deviation: discrepancies exemplified by i. in Figure 2j,l are in the region of uniformly

magnetised FM and often accompanied by slight impressions in the adjacent FM layer. Discrepancies exemplified by ii. in Figure 2l are inside the imprinted spin textures and deviate completely from the FM spin configuration. The reason for these discrepancies is likely that the FM-AFM exchange interaction is not strong enough to set all the grains, which is demonstrated in SM - stronger exchange strength improves the FM-AFM spin texture conformity while zero exchange interaction results in the AFM having a completely random domain structure. It is also possible that some of the i. type discrepancies are residual imprintings of FM Sks that moved or were annihilated during the field-cooling (compare the FM Sk locations in Figures 2a and 2j). Finally, the last simulation step shown in Figure 2j-l is the removal of the external field, which causes only minor changes to the spin textures throughout the stack, demonstrating the zero-field stability of the imprinted localised AFM spin textures. In summary, this set of simulations shows that i) spin textures (here Sks) initially nucleated in a FM layer can be imprinted across the interface onto an AFM layer by following a thermal cycling protocol, ii) the imprinted textures penetrate into the bulk of the AFM and iii) they are stable at remanence. Note that these conclusions are valid for any final temperature below T_N, including room temperature in our case (see SM). The robustness and universality of our results is further demonstrated in SM where we show the imprinting of another spin texture, namely maze domains, from the FM into the AFM layer.

The exact nature and morphology of the imprinted textures (Figure 3) is discussed next. The radii of the Sks in the FM (Figure 3a-b) range from $\sim$ 10 to 20 nm and their shape is rather irregular, most likely due to the pinning by the grain boundaries of the AFM layer (see SM for the conformity between the Sk shapes and the AFM grain structure). The variation of the spin components s_x, s_y, and s_z across the cross-section shows behaviour characteristic of a Néel type Sk (Figure 3d-f), which is in good agreement with the interfacial DMI, and its strength being above the critical strength for a Bloch to Néel domain wall transition ($D_c = 4\mu_0 M_s^2 t \ln 2/2\pi^2$). The s_x and s_z components can be fitted using $\cosh^{-1}(\pi[x-x_0]/\Delta)$ and $\tanh(\pi[x-x_0]/\Delta)$ functions, respectively, where x_0 is the domain wall centre location and Δ is the domain wall width. For the selected skyrmion, $\Delta \sim 8.4$ nm, which is in the same order of magnitude as expected by theory [30]. The winding number of the individual Sks in the FM layer in Figure 2j is Q=1 and for the five entire Sks Q=5 (calculation in SM).

At the AFM interface (IrMn 1 in Figure 3), the s_x, s_y, and s_z components show average behaviour that corresponds to that of the FM layer, providing further support for the spin texture imprinting. In SM we show that for a simulation stack without FM-AFM interfacial exchange

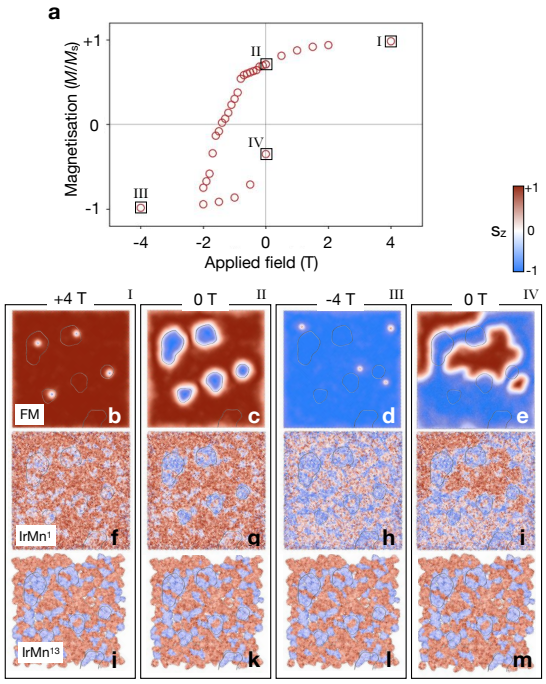

FIG. 4. (Color Online) (a) Field-dependence of the FM magnetisation, normalized (M/Ms), at 0 K and (b-m) snapshots of the evolution of the spin structures during the field-sweep, in the FM (b), AFM at the interface (c, IrMn 1) and AFM in the core (d, IrMn 13). The snapshots are taken at positive saturation (1.), forward remanence (2.), negative saturation (3.) and backward remanence (4.). The contours of the FM Sks in 2j) are superimposed to all images, as visual guides.

coupling there is no correspondence between s_i of the FM and AFM layers. The increased noise is likely due to the strong anisotropy of γ-$IrMn_3$, interfacial intermixing, and the interfacial magnetisation comprising of a reversible and irreversible component [31] where the former follows the FM spins while the latter is strongly coupled to the AFM bulk. The different behaviors of these two components are also observed during the field cycling as will be discussed later. From the topmost AFM layer the spin texture imprinting propagates down to the bottom of the AFM layer with the polarity of the texture alternating between each consecutive monolayer, as shown in Figure 1. This is in a good agreement with the typical tetrahedral 3Q symmetry of the AFM ordering of γ-$IrMn_3$ [32]. In the bulk of the AFM (IrMn 13 in Figure 3) the noise is reduced, as there is no need to accommodate for intermixing and the resulting non IrMn AFM bonds, but some noise remains from the anisotropy of γ-$IrMn_3$. The behavior of the s_z component agrees well with that of the FM layer, with the only exception being that the domain walls are narrower as they

follow the AFM grain boundaries. The penetration depth of the imprinting, down to the last layer IrMn 34 which is 5 nm away from the interface, is in good agreement with experimental reports on vortices in CoO and NiO [19] and exchange springs in γ-$IrMn_3$ [**?**], which could propagate over the whole AFM thickness.

Next, we study the effect of cycling the external field (oriented along the film normal) on the spin textures throughout the simulation stack. As expected, the hysteresis loop (Figure 4a) exhibits a shift of ~ -0.7 T towards negative fields due to the exchange bias originating from the uncompensated, irreversible interfacial Mn spins [23]. The spin texture evolution, on the other hand, strongly depends on the layer. The FM layer follows the field, nearly saturating at strong fields (Figure 4b,d) and gradually reversing at intermediate fields by the expansion of Sk bubbles (SM). The AFM bulk, on the other hand, remains unchanged throughout the field cycle as seen in Figure 4j-m. This can also be seen in the fact that at remanence, the FM layer (Figure 4c,e) adopts a configuration that conforms with that of the AFM layer. The AFM interface comprises a reversible component that follows the FM and an irreversible component that abides by the AFM bulk, and therefore shows a behaviour that is a mixture of the two (Figure 4f-l). This shows that the imprinted local spin textures remain unaltered in the AFM bulk and partially at the interface even after the original Sks in the FM layer are annihilated. This means that we are able to transform a system with Sks in the FM layer and no spin textures in the AFM (Figure 2a-c) to a system with no Sk in the FM layer but pre-defined spin textures in the AFM layer (Figure 4g-i) using consecutive thermal and field cycling processes. This opens up perspectives for the further study of spintronic properties of isolated, localised spin textures in an AFM.

In conclusion, we have theoretically demonstrated nucleating of predefined, localised spin textures in antiferromagnetic γ-$IrMn_3$ by transferring spin textures from an adjacent exchange-coupled ferromagnet. This transfer of different spin textures (here skyrmions) was realized by a thermal cycling procedure and it was shown to extend beyond the interface through the entire thickness of the antiferromagnet (here 5 nm). The imprinted textures showed remarkable stability against field perturbations and the imprinting efficiency as well as the morphologies of the imprinted textures were shown to depend on various material parameters. This work offers a solution for overcoming the challenge of nucleating localised real-space spin textures in compensated magnets with zero net magnetisation, promoting the extension of the study of topology beyond ferromagnets.

This study was partially supported by the France-UK Alliance Hubert Curien programme

(PHC) (Grant No. 46298XC) and the UK EPSRC programme (Grant No. EP/V007211/1). This work used the ARCHER2 UK National Supercomputing Service (https://www.archer2.ac.uk).

[1] D. Xiao, M.-C. Chang, and Q. Niu, Reviews of Modern Physics **82** (2010).

[2] B. Göbel, A. Mook, J. Henk, and I. Mertig, The European Physical Journal B **91** (2018).

[3] H. Chen, Q. Niu, and A. MacDonald, Physical Review Letters **112** (2014).

[4] L. Šmejkal, R. González-Hernández, T. Jungwirth, and J. Sinova, Science Advances **6** (2020).

[5] S. Nakatsuji, N. Kiyohara, and T. Higo, Nature **527** (2015).

[6] Z. Feng, X. Zhou, L. Šmejkal, L. Wu, Z. Zhu, H. Guo, R. González-Hernández, X. Wang, H. Yan, P. Qin, X. Zhang, H. Wu, H. Chen, Z. Meng, L. Liu, Z. Xia, J. Sinova, T. Jungwirth, and Z. Liu, Nature Electronics **5** (2022).

[7] H. Reichlová, R. L. Seeger, R. González-Hernández, I. Kounta, R. Schlitz, D. Kriegner, P. Ritzinger, M. Lammel, M. Leiviskä, V. Petříček, P. Doležal, E. Schmoranzerová, A. Bad'ura, A. Thomas, V. Baltz, L. Michez, J. Sinova, S. T. B. Goennenwein, T. Jungwirth, and L. Šmejkal, (unpublished).

[8] J. Železný, Y. Zhang, C. Felser, and B. Yan, Physical Review Letters **119** (2017).

[9] A. Bose, N. J. Schreiber, R. Jain, D.-F. Shao, H. P. Nair, J. Sun, X. S. Zhang, D. A. Muller, E. Y. Tsymbal, D. G. Schlom, and D. C. Ralph, Nature Electronics **5** (2022).

[10] H. Bai, L. Han, X. Feng, Y. Zhou, R. Su, Q. Wang, L. Liao, W. Zhu, X. Chen, F. Pan, X. Fan, and C. Song, Physical Review Letters **128** (2022).

[11] V. Baltz, A. Manchon, M. Tsoi, T. Moriyama, T. Ono, and Y. Tserkovnyak, Reviews of Modern Physics **90** (2018).

[12] L. Šmejkal, Y. Mokrousov, B. Yan, and A. H. MacDonald, Nature Physics **14** (2018).

[13] X. Zhang, Y. Zhou, and M. Ezawa, Scientific Reports **6** (2016).

[14] J. Barker and O. A. Tretiakov, Physical Review Letters **116** (2016).

[15] B. Göbel, A. Mook, J. Henk, and I. Mertig, Physical Review B **96** (2017).

[16] C. Akosa, O. Tretiakov, G. Tatara, and A. Manchon, Physical Review Letters **121** (2018).

[17] R. Khoshlahni, A. Qaiumzadeh, A. Bergman, and A. Brataas, Physical Review B **99** (2019).

[18] G. Salazar-Alvarez, J. J. Kavich, J. Sort, A. Mugarza, S. Stepanow, A. Potenza, H. Marchetto, S. S. Dhesi, V. Baltz, B. Dieny, A. Weber, L. J. Heyderman, J. Nogués, and P. Gambardella, Applied Physics Letters **95** (2009).

[19] J. Wu, D. Carlton, J. S. Park, Y. Meng, E. Arenholz, A. Doran, A. T. Young, A. Scholl, C. Hwang, H. W. Zhao, J. Bokor, and Z. Q. Qiu, Nature Physics **7** (2011).

[20] K. G. Rana, R. L. Seeger, S. Ruiz-Gómez, R. Juge, Q. Zhang, K. Bairagi, V. T. Pham, M. Belmeguenai, S. Auffret, M. Foerster, L. Aballe, G. Gaudin, V. Baltz, and O. Boulle, Applied Physics Letters **119** (2021).

[21] O. Boulle, J. Vogel, H. Yang, S. Pizzini, D. de Souza Chaves, A. Locatelli, T. O. Menteş, A. Sala, L. D. Buda-Prejbeanu, O. Klein, M. Belmeguenai, Y. Roussigné, A. Stashkevich, S. M. Chérif, L. Aballe, M. Foerster, M. Chshiev, S. Auffret, I. M. Miron, and G. Gaudin, Nature Nanotechnology **11** (2016).

[22] H. Yang, A. Thiaville, S. Rohart, A. Fert, and M. Chshiev, Physical Review Letters **115** (2015).

[23] S. Jenkins, W. J. Fan, R. Gaina, R. W. Chantrell, T. Klemmer, and R. F. L. Evans, Physical Review B **102** (2020).

[24] S. Jenkins, R. W. Chantrell, T. J. Klemmer, and R. F. L. Evans, Physical Review B **100** (2019).

[25] S. Jenkins, R. W. Chantrell, and R. F. L. Evans, Physical Review Materials **5** (2021).

[26] R. F. L. Evans, W. J. Fan, P. Chureemart, T. A. Ostler, M. O. A. Ellis, and R. W. Chantrell, Journal of Physics: Condensed Matter **26** (2014).

[27] J. D. Alzate-Cardona, D. Sabogal-Suárez, R. F. L. Evans, and E. Restrepo-Parra, Journal of Physics: Condensed Matter **31** (2019).

[28] G. Vinai, J. Moritz, S. Bandiera, I. L. Prejbeanu, and B. Dieny, Applied Physics Letters **104** (2014).

[29] S. Jenkins, R. W. Chantrell, and R. F. L. Evans, Physical Review B **103** (2021).

[30] X. S. Wang, H. Y. Yuan, and X. R. Wang, Communications Physics **1** (2018).

[31] J. Nogués and I. K. Schuller, Journal of Magnetism and Magnetic Materials **192** (1999).

[32] A. Sakuma, K. Fukamichi, K. Sasao, and R. Y. Umetsu, Physical Review B **67** (2003).

[33] L. Szunyogh, B. Lazarovits, L. Udvardi, J. Jackson, and U. Nowak, Physical Review B **79** (2009).

[34] R. J. Wakelin and E. L. Yates, Proceedings of the Physical Society. Section B **66** (1953).

[35] J. M. D. Coey, *Magnetism and Magnetic Materials* (Cambridge University Press, 2010).

[36] L. Frangou, S. Oyarzún, S. Auffret, L. Vila, S. Gambarelli, and V. Baltz, Physical Review Letters **116** (2016).

[37] B. Berg and M. Lüscher, Nuclear Physics B **190** (1981).

[38] M. Böttcher, S. Heinze, S. Egorov, J. Sinova, and B. Dupé, New Journal of Physics **20** (2018).

SUPPLEMENTARY MATERIAL

PARAMETERS USED FOR THE SIMULATIONS DESCRIBED IN THE MAIN TEXT

Onsite and intersites simulation parameters

Here, we list all the relevant parameters used in our simulations. The onsite magnetic properties of each magnetic element in the simulation stack are listed in Table S1, where μ_s is the atomic magnetic moment, D is the DMI coefficient, and k_N is the Néel pair anisotropy coefficient. The intermixing value refers to the fraction of the given layer that is intermixed with the layer below. For the permalloy layer ($Ni_{80}Fe_{20}$), μ_s was calculated from the saturation magnetisation M_s of $\sim 8.6 \times 10^5$ A/m using $\mu_s = M_s a^3/n_{at}$[26], where a is the lattice constant and n_{at} is the number of atoms in the unit cell. For Co the values were obtained from ref. [26] and for γ-$IrMn_3$ from ref. [23]. The intersite exchange (J_{ij}) and DMI (D) interactions are listed in Table S2. For $Ni_{80}Fe_{20}$ the J_{ij} is calculated from the expected Curie temperature T_c of ~ 900 K using $J_{ij} = 3k_B T_c/\varepsilon z$, where ε is the spin-wave mean-field correction and z is the number of nearest neighbours[26]. For Co the values are obtained from ref. [26] and for γ-$IrMn_3$ from *ab initio* calculations[33].

Parameter	$Ni_{80}Fe_{20}$	Co	Mn
μ_s (μ_B)	1.05	1.72	2.6
k_N (10^{-22} J/atom)	–	0.025 (Pt)	-4.22 (Ir)
Intermixing	2.5 %	2.5 %	5 %

Table S1. Parameters used in the main paper simulation for each magnetic elements.

	NiFe	Co	Pt	Mn
NiFe	3.8	5	0.5*	1.21
Co	5	6.1	0.5*	1.21
Pt	0.5*	0.5*	–	–
Mn	1.21	1.21	–	-6.4 (NN) 5.1 (NNN)

Table S2. Exchange (J_{ij}) and DMI* coefficients (D) (10^{-21} J/link) between the different magnetic elements in the stack. NN is for nearest neighbors and NNN for next nearest neighbors

Critical temperatures of the simulation stack

In this set of simulations, we determined the various critical temperatures of the simulation stack (Figure S1a). We found that the Curie temperature of the hybrid FM layer (NiFe/Co) is ~ 900 K, which is in agreement with both experimental values (~ 870 K [34][35]) and the value of exchange constant set in the simulations. We also determined that the Néel temperature of the γ-$IrMn_3$ layer is ~ 510 K, which is in agreement with the experimental values [36] for a 5 nm thick γ-$IrMn_3$.

In Figure S1b we show the room temperature spin textures in the FM layer, AFM interface and AFM bulk of the main paper simulation stack. The imprinting is clearly visible in the AFM bulk and also discernible at the AFM interface, implying that we can realize imprinting of spin textures onto the AFM bulk at any temperature below T_N, including the room temperature, and cryogenic temperatures are not necessary.

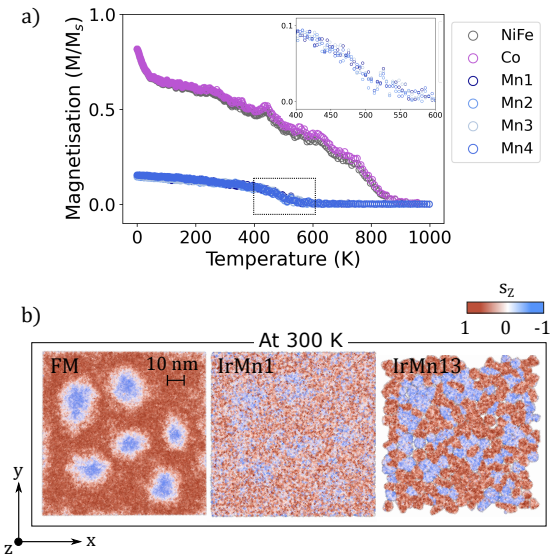

Figure S1. (Color Online) a) Temperature dependence of the magnetisation (M/Ms) of each magnetic material in the stack, consisting of a hybrid NiFe/Co FM single crystal coupled to a γ-$IrMn_3$ AFM through ultrathin Pt layer. The data were obtained from a field-cooling simulation running down from 1000 to 0 K. Note: for the γ-$IrMn_3$ layer the 4 sublattice magnetisations are plotted separately. The inset is a zoom on the behaviour of these Mn sublattices near the Néel temperature. b) The room-temperature spin textures in the FM layer, AFM interface (IrMn1) and AFM bulk (IrMn13) of the main paper simulation stack.

Grain structure of the γ-$IrMn_3$ layer

The grain structure of the γ-$IrMn_3$ layer is shown in Figure S2a. The nominal average size of the grains was set as 5 nm with a variance of 0.5 and the grain spacing was set as 0.75 nm. The grain structure is created using a Voronoi construction where the seed points are generated in a hexagonal grid and slightly moved around based on the standard deviation of the grain size distribution. The real grain size distribution is plotted in Figure S2c showing an average grain size of ~ 4.5 nm. In Figure S2b it can be seen that the shape of the FM Sks follows closely the grain boundaries of the AFM, explaining the irregular shape of the Sks.

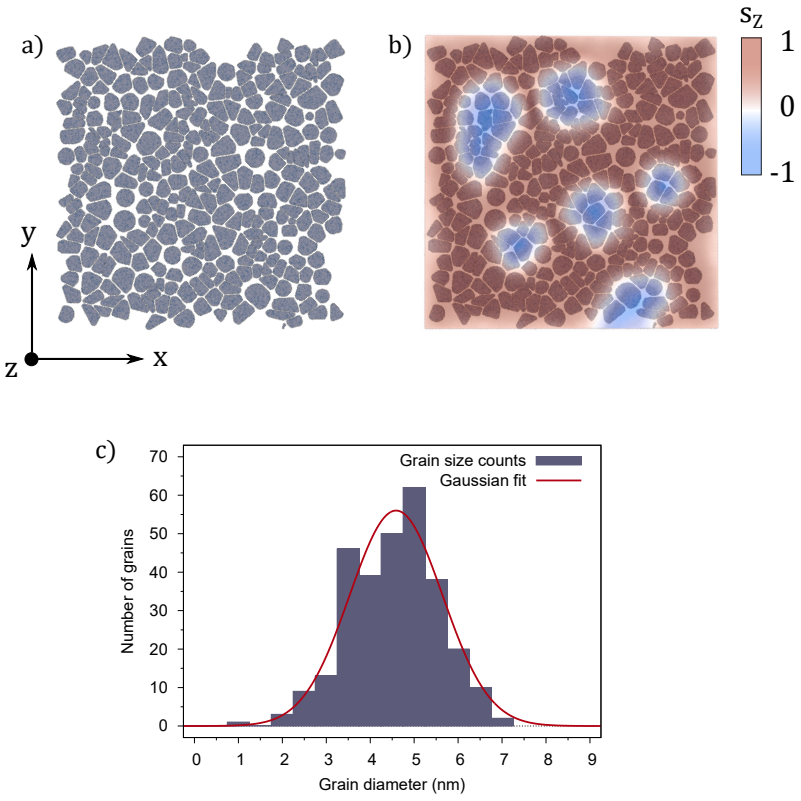

Figure S2. (Color Online) a) The bare grain structure of the AFM layer created using a Voronoi construction. b) Overlaying the FM layer spin structure and the bare grain structure shows that the irregular shape of the skyrmions in the former follow the grain boundaries of the latter. c) The actual grain size distribution for a system with nominal average grain size of 5 nm. A gaussian fit is for the distribution is also plotted, showing an actual average grain size of ~ 4.5 nm.

Native spin configuration of the γ-$IrMn_3$ layer

In this control simulation, shown in Figure S3, we show the native spin structure of the AFM layer in the absence of exchange coupling to the FM layer and thus the absence of imprinting of the FM spin texture (here, a domain wall). Instead, the grains within the AFM layer are randomly set providing information on the native spin configuration without the influence of the FM. This is also visible more quantitatively in Figure S3c-f as the spin components (s_i) of the IrMn1, IrMn4, and IrMn5 layers do not follow those of the FM layer.

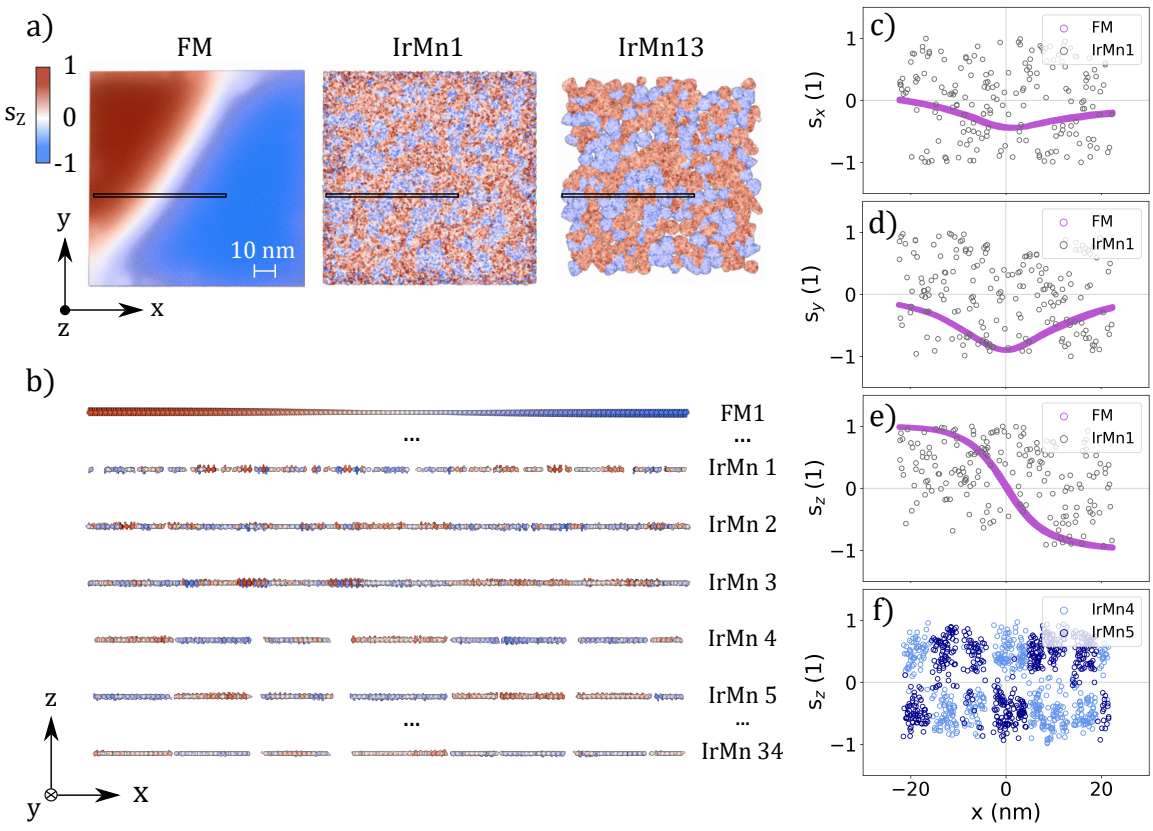

Figure S3. (Color Online) a) The spin texture of the FM (NiFe/Co) layer and the AFM interface (IrMn1) and bulk (IrMn13) at 0 K and 0 T. b) Cross-section of the domain wall as marked by the black square in a). The spin configuration is shown for an FM monolayer and consecutive IrMn monolayers starting from the interface. c-f) Evolution of the spin components of the FM monolayer and selected IrMn layers across the cross-section shown in a) and b). It can be seen that there is no clear correlation between the FM and AFM spin components showing the absence of imprinting.

INFLUENCE OF VARIOUS SIMULATION PARAMETERS ON IMPRINTING EFFICIENCY AND MORPHOLOGY

Here we detail the impact of changing some of the simulation parameters on how efficiently spin textures are imprinted from FM to the AFM. We show that the most critical parameters for the imprinting efficiency is the interfacial exchange coupling strength as well as the intermixing, as these two govern how strongly the interfacial AFM spins couple with the FM spins and therefore how strongly inclined they are to copy the spin orientations of the latter. The other parameters like field-cooling conditions (initial temperature, zero vs non-zero field strength) and DMI strength influence the morphologies of both the initial FM spin textures as well as the imprinted AFM spin textures. For each case we ran the same simulation steps as detailed in the main text, and the snapshots in all the figures are taken after the final simulation step of removing the external field so at 0 K and 0 T.

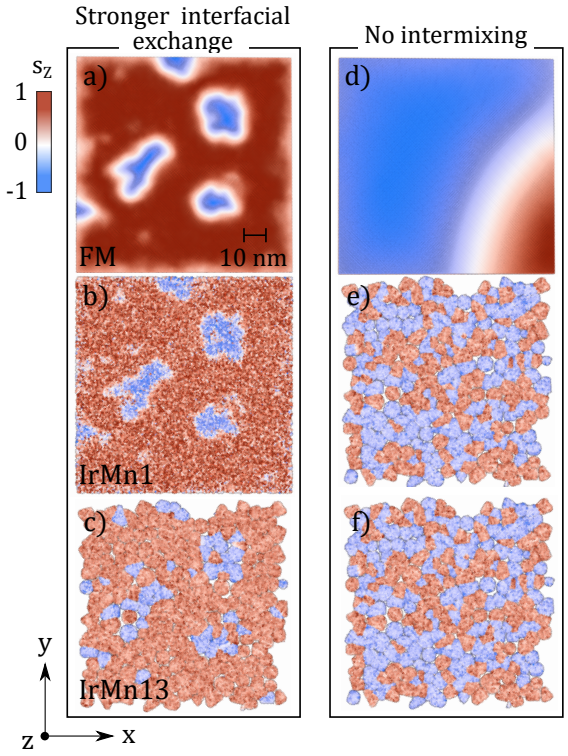

Figure S4. (Color Online) The effect of stronger interfacial exchange coupling (a-c) and removal of the interlayer intermixing (d-f) on the spin texture imprinting. The former improves the imprinting efficiency while the latter results in the absence of imprinting.

FM-AFM exchange interaction strength

Here, we verified that stronger coupling between the two layers leads to a more efficient imprinting (Figure S4a-c). For the simulations, we used an exchange interaction strength of 3.21×10^{-21} J/link between the FM and AFM layers, which is three times stronger compared to the simulations discussed in the main text. Two notable differences to the results of the main stack can be detected. First, the shape of the FM skyrmions is increasingly irregular, most likely due to the AFM grain boundaries having a stronger influence on the FM spins. Secondly, there are fewer discrepancies between the spin structure of the FM layer and that of the AFM layer, resulting from the increased tendency of the AFM spins to follow the FM spins. We note that in addition to imprinting efficiency also the exchange bias dragging will be more efficient, making it less likely to obtain an isolated AFM Sk.

Layers intermixing

In the control simulations shown in Figure S4(g-i) we show that layer intermixing is essential for magnetically coupling the FM and AFM layers in our system. This is because the FM and AFM layers are separated by a thin Pt layer that provides both the interfacial DMI and perpendicular magnetic anisotropy (see main text). In the absence of intermixing the FM and AFM layers will not come into direct contact and effectively, will not interact. This means that removing intermixing has the same impact as removing the interfacial exchange coupling, where the AFM magnetic configuration sets in a random configuration independently on the FM configuration. Implementing longer-range exchange interactions such as RKKY coupling would alter the effect of layer intermixing, without changing the physical ideas discussed in the text.

WINDING NUMBER OF THE SKYRMION BUBBLES

The winding number Q for a discretized system is calculated by summing up the topological charge density q per a square cell:

$$q(x^*) = \frac{1}{4\pi}[(\sigma A)(s_1, s_2, s_3) + (\sigma A)(s_1, s_3, s_4)], \tag{2}$$

$$\sigma A(s_j, s_k, s_l) = 2\tan^{-1}\left(\frac{\mathbf{s}_j \cdot \mathbf{s}_k \times \mathbf{s}_l}{1 + \mathbf{s}_j \cdot \mathbf{s}_k + \mathbf{s}_j \cdot \mathbf{s}_l + \mathbf{s}_k \cdot \mathbf{s}_l}\right), \tag{3}$$

where $\mathbf{s}_i$ is the magnetisation vector at site i [37, 38].

As seen in Figure S5 we have calculated the winding number for the FM layer shown in the main paper Figure 2j using the equations given above and obtained $Q \approx 5.4$. This corresponds well to the presence of five entire and one incomplete skyrmions in the layer. We have also calculated the winding number of the individual skyrmion bubbles separately and confirmed that $Q \approx 1$.

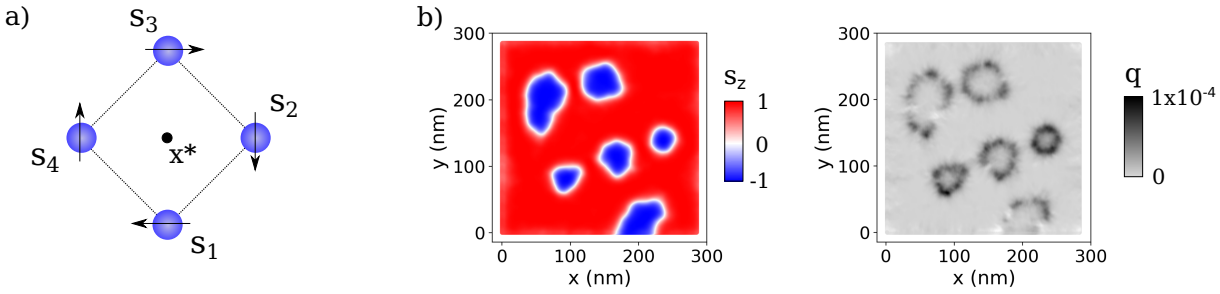

Figure S5. (Color Online) a) The schematics for calculating the topological charge density q of a discrete lattice made up of square unit cells. The total topological charge Q is the sum of q over the entire lattice. b) The topological charge density calculated for the FM layer shown in the main paper.